y 1994

Chapter 10

Project WIND Numerical Simulations with the Tel Aviv Model: PSU–NCAR Model Run at Tel Aviv University

P. ALPERT AND M. TSIDULKO

Department of Geophysics and Planetary Sciences, Tel Aviv University, Tel Aviv, Israel

10.1. Description of the model

The model was developed by Anthes, Warner, Ying-Hwa Kuo, and their colleagues at the National Center for Atmospheric Research (NCAR) and The Pennsylvania State University (PSU).

Equations: The version of the PSU–NCAR Mesoscale Model (MM4) that was used in the studies is described along with the full set of equations in Anthes et al. (1987) and Hsie (1987). These are summarized in the appendix. The model is hydrostatic. The closure physics on the subgrid are first order, and detailed boundary parameterization is according to Blackadar's formulation. A grid-scaled diffussivity is also included for stability.

Dimensionality: One-, two-, and three-dimensional versions of this code have been developed.

Grid: Typical grid spacing of this code is 10–80-km resolution, but some runs have been made with resolution down to 5 km. In the vertical, grid spacing is from 30 m near the ground to 1 km higher up. The standard version has 16 layers, but more levels can be used. The horizontal domain is variable and is typically less than 5000 km on a side. The grid is a staggered Arakawa B grid. The coordinate system uses height pressure coordinates in the vertical and either polar stereographic, Lambert conformal, or Mercator map projections.

Analysis methodology: The analysis methodology uses National Meteorological Center (NMC) or European Centre for Medium-Range Weather Forecasts (ECMWF) analyses enhanced by significant and standard-level radiosonde data plus artificial (subjective) soundings generated by satellite data. Here, only Project WIND radiosonde data were used.

Model initialization procedure: Model initialization procedures include normal-mode initialization, boundary nudging, balance equations, 4D data assimulation, and adiabatic and diabatic processes.

Solution technique: The finite-difference method approximately conserves mass, momentum, and total energy. The staggered grid was shown to give significantly better results in tropical cyclone simulations; increased accuracy was attributed to better pressure gradient and horizontal divergence calculations. The p^*u and p^*v variables are calculated at the so-called dot points, and all other variables are calculated at offset cross points. Several options exist for boundary treatment. The usual upper boundary condition is $\dot{\sigma} = 0$. There are five lateral boundary condition options: fixed, time dependent, time dependent in/outflow, sponge, and Davies relaxation.

In the following, only fixed (summer) or time-dependent (winter) options were used.

Surface boundary treatment: The surface boundary treatment enforces $d\sigma/dt = 0$.

Soil treatment: Ground temperature is obtained from a surface energy budget. Over land, the surface energy budget of Blackadar (Zhang and Anthes 1982) is used to calculate the ground temperature through a temperature force/restore slab soil model.

Canopy and land-use treatment: Momentum and energy parameterizations consistent with Blackadar's planetary boundary layer (PBL) are used for a variety of land-use and vegetative combinations.

Special conditions: The model has been run under various conditions as described by Anthes (1990).

Radiation parameterization: Shortwave transmitivity is according to Benjamin (1983), and cooling rate treatment is according to Paltridge and Platt (1981).

Hydrological cycle: Four options exist for the moisture handling: vapor treated as a passive variable; excess water vapor over RH_c removed as precipitation; cumulus parameterization following Kuo (1974) and Anthes (1977), with total convective heating proportional to the moisture convergence in a vertical column (this is the option used here); and an explicit prognostic scheme for water vapor, cloud water, and rainwater (Hsie and Anthes 1984).

Coding practices: Fortran 77, vectorization, modularity, Cray XMP, YMP, CDC 990, IBM 320, and visualization on a workstation. Here, the model was run on the IBM workstation.

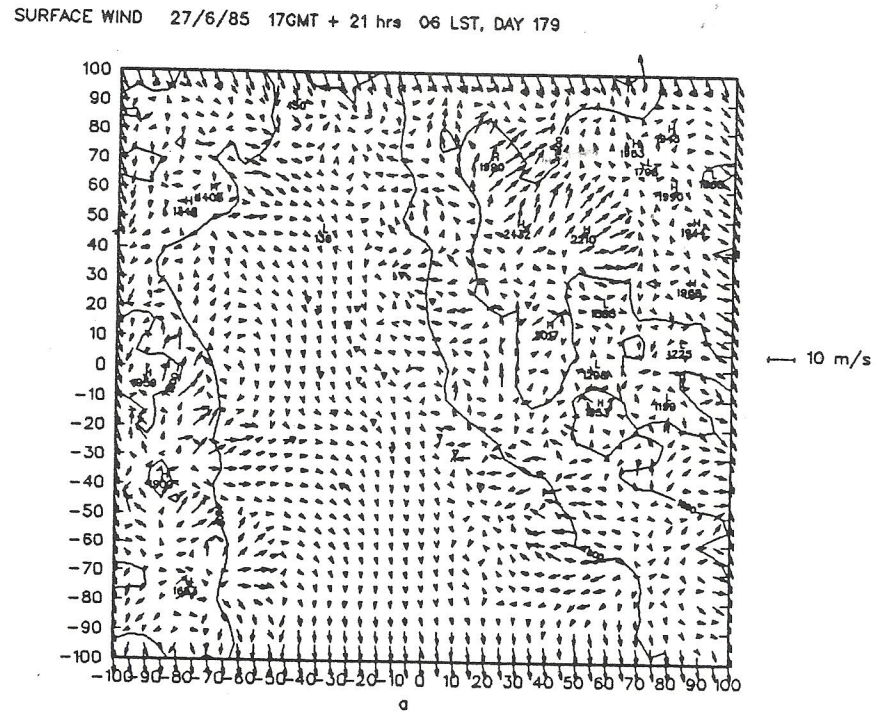

FIG. 10.1. Surface wind vectors for (a) 0600 and (b) 1500 PST 27 June 1985 over the full simulation region, in Sacramento Valley. Topographical contours of 800 and 1800 m are shown. Wind scale is indicated on the right.

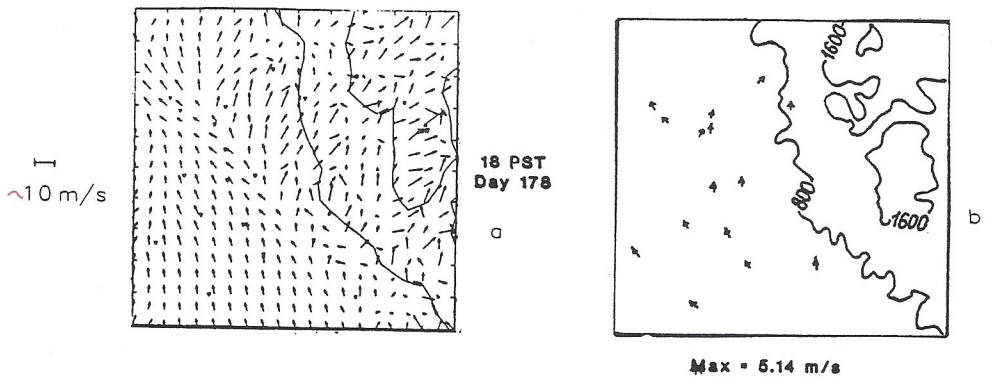

FIG. 10.2. Surface wind vectors from (a) model and (b) observations at 1800 PST over the inner 80 km × 80 km domain. Topographical contours as in Fig. 10.1. Wind scale indicated.

10.2. Setup for WIND simulations

In the following, MM4 version 7 as described by Anthes et al. (1987) was applied, with 16 σ levels at the approximate half σ levels of 0, 5, 15, 28, 55, 230, 450, 920, 1900, 3200, 4900, 6600, 8500, 10 700 and 14 000 m. Top model pressure p_t was 10 mb and a 10-s time step was necessary with the 5-km horizontal interval. Ten computer hours were required for a grid of 41 × 41 × 16 run on a workstation IBM 320 for a 24-h simulation.

For the initial fields the four or five available radiosondes (summer or winter) were interpolated. No use of any surface data was attempted at this stage. The lateral boundary conditions were fixed or updated (in the winter phase) where the time variation followed the 12-h interpolated fields based on the five available radiosondes.

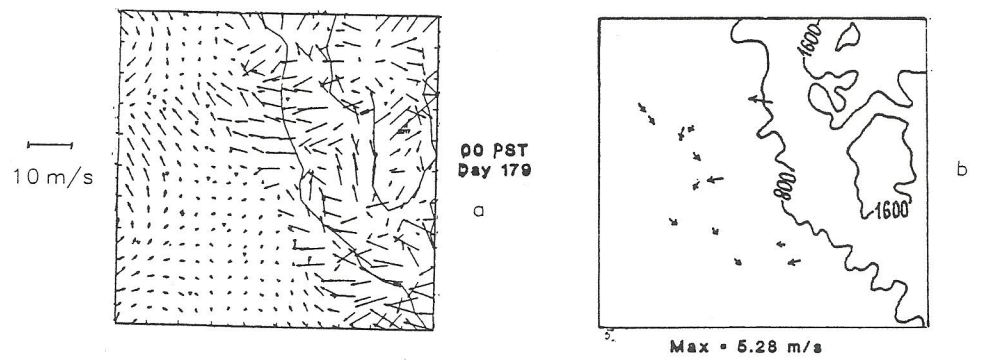

FIG. 10.3. As in Fig. 10.2 except for 0000 PST.

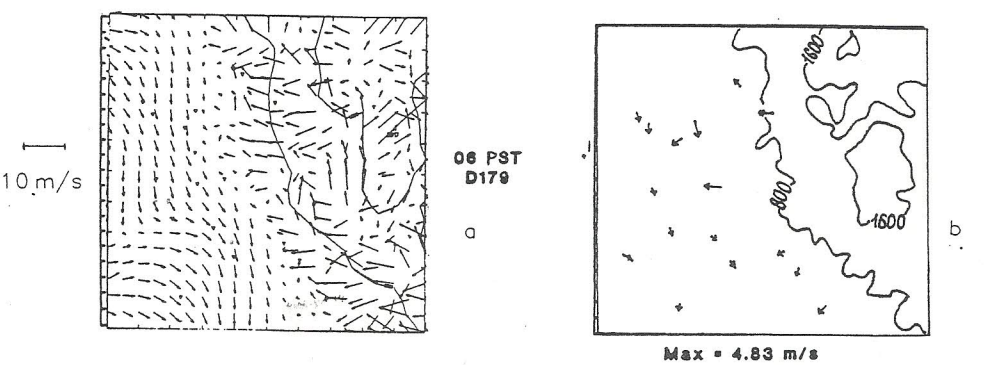

FIG. 10.4. As in Fig. 10.2 except for 0600 PST.

TABLE 10.1. Description of land-use categories and physical parameters for summer (15 April–15 October) and winter (15 October–15 April).

Land-use integer identification	Land-use description	Albedo (%)		Moisture availability (%)		Emissivity (percent at 9 μm)		Roughness length (cm)		Thermal inertia (cal cm^{-2} K^{-1} s$^{-1/2}$)	
		summer	winter	summer	winter	summer	winter	summer	winter	summer	winter
1	Urban land	18	18	5	10	88	88	50	50	0.03	0.03
2	Agriculture	17	23	30	60	92	92	15	5	0.04	0.04
3	Range-grassland	19	23	15	30	92	92	12	10	0.03	0.04
4	Deciduous forest	16	17	30	60	93	93	50	50	0.04	0.05
5	Coniferous forest	12	12	30	60	95	95	50	50	0.04	0.05
6	Mixed forest and wetland	14	14	35	70	95	95	40	40	0.05	0.06
7	Water	8	8	100	100	98	98	0.0001	0.0001	0.06	0.06
8	Marsh or wetland	14	14	50	75	95	95	20	20	0.06	0.06
9	Desert	25	25	2	5	85	85	10	10	0.02	0.02
10	Tundra	15	70	50	90	92	92	10	10	0.05	0.05
11	Permanent ice	55	70	95	95	95	95	5	5	0.05	0.05
12	Tropical or subtropical forest	12	12	50	50	95	95	50	50	0.05	0.05
13	Savannah	20	20	15	15	92	92	15	15	0.03	0.03

10.3. Summer phase I results

Only four radiosondes were available at the initial time (1000 PST) on the 27 June 1985. The lateral boundary conditions were kept constant.

a. Wind simulations

Figures 10.1a and 10.1b show the surface wind results for 0600 and 1500 PST corresponding to 21 and 6 h of simulation. The total domain is shown and the katabatic (downvalley) flow at night as well as the anabatic (upvalley) flow during day are simulated. Comparison with observations for the inner 80 km × 80 km domain is shown in Figs. 10.2a,b, 10.3a,b, and 10.4a,b for 1800, 0000, and 0600 PST, respectively. The model is capable of predicting some small-scale flow features like wind turning from southeast to southwest over the valley as moving from south to north at 1800 PST (Figs. 10.2a,b). Also, a relatively strong easterly flow (~8 m s^{-1}) into the valley at midnight is predicted. Other features are not so well reproduced. For instance, the location of the southeast–northwest convergence line in the valley seems to be predicted slightly farther to the east (~10 km). In the following sections, some of the model sensitivities to land-use variability, subscale topography, and moisture initialization are explored.

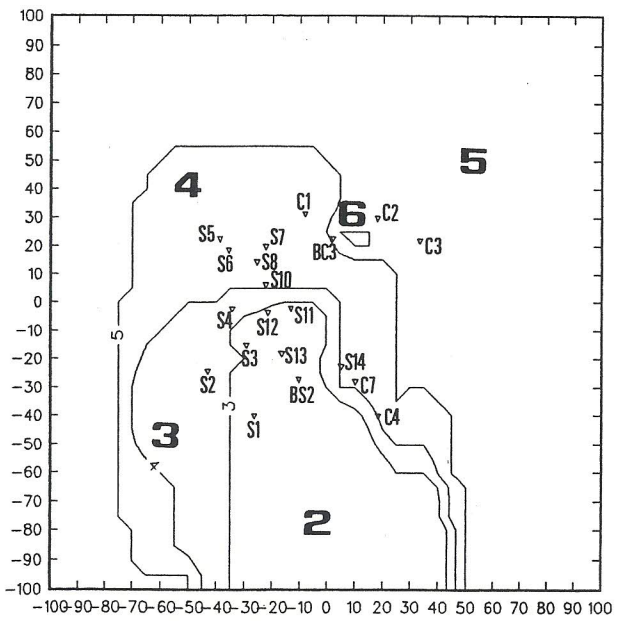

FIG. 10.5. The land-use categories over the model domain based on NCAR classification over a grid of (1/6° × 1/4°). Stations' locations are indicated by triangles. Physical parameters for each category are in Table 10.1.

b. Land-use variability

Figure 10.5 shows the land-use categories over the model domain as given by the NCAR land-use file. Resolution of the land-use (LU) set is coarser than the model grid (1/6° × 1/4°). Most of the region is characterized by LU category 5—coniferous forest; LU = 4—deciduous forest; LU = 3—grassland or LU = 2—agricultural area. Table 10.1 summarizes the physical parameters for the various categories. Two simulations were performed: one with a constant LU category 3, and the other with the variable LU as in Fig. 10.5. Figures 10.6a,b and 10.7 show the surface latent and sensible heat fluxes (LH and SH) and the Bowen ratio (BR), respectively, where

$$\mathrm{BR} = \frac{\mathrm{SH}}{\mathrm{LH}},$$

for the constant LU run, and Fig. 10.8 shows the BR field for the variable land use. One can notice drastic changes in the BR field over some regions. For instance,

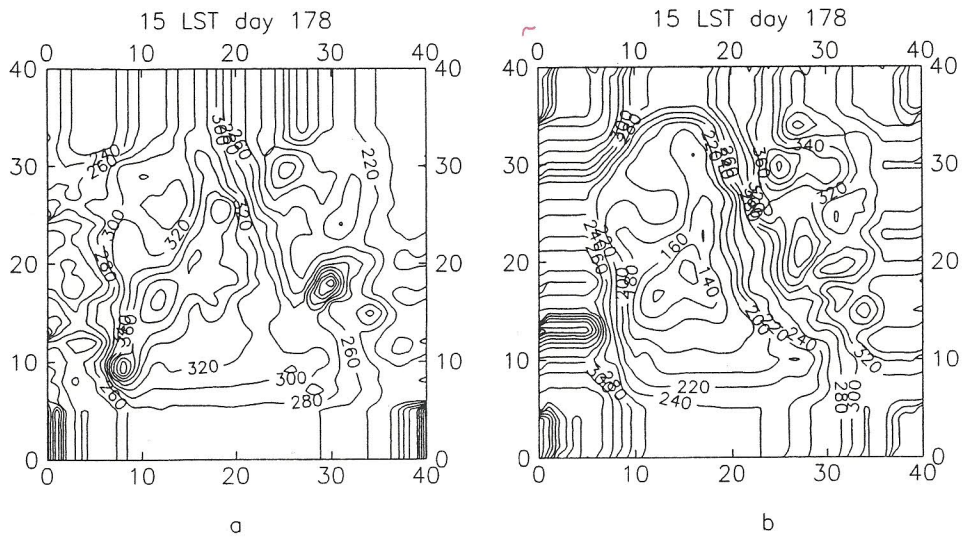

FIG. 10.6. The surface (a) latent and (b) sensible heat fluxes (W m^{-2}) at 1500 PST, for the constant land-use run.

over the southern part of the valley (grid point 20, 4) BR value drops from 0.9 in the constant LU run (Fig. 10.7) to 0.4 with the variable LU. The reason for this is clear; the constant LU category 3 replaces over this location the moister agricultural area with LU = 2, and so the surface moisture availability is too low (15% instead of 30%, Table 10.1). Consequently, the LH is underestimated leading to a near doubling of BR. Obviously, there are other effects like the too low roughness (12 cm instead of 50 cm, Table 10.1) with LU = 4, where the range grassland replaces the deciduous forest in the constant LU = 3 run. The partition between LH and SH is most important in driving the thermally induced circulations over the valley, and a doubling of the Bowen ratio certainly represents a major change in this partition.

c. *Topographical resolution*

Figures 10.9a–d and 10.10a–d show the 10-m diurnal variations for stations S10 and S11. Although the two stations are quite close, separated by only about 10 km

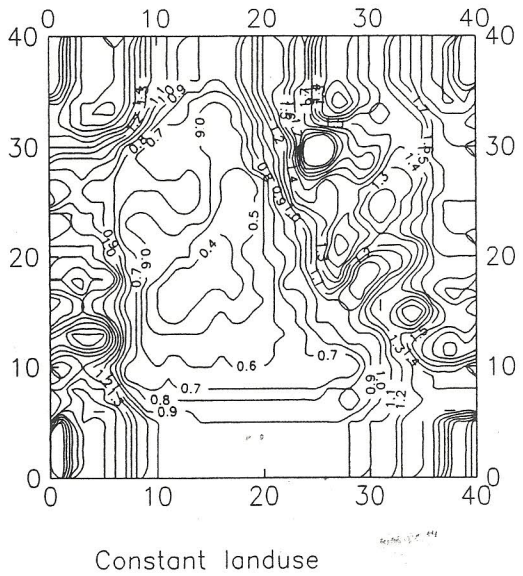

FIG. 10.7. The Bowen ratio (SH/LH) for the constant land use at 1500 PST. Coordinate numbers indicate grid values.

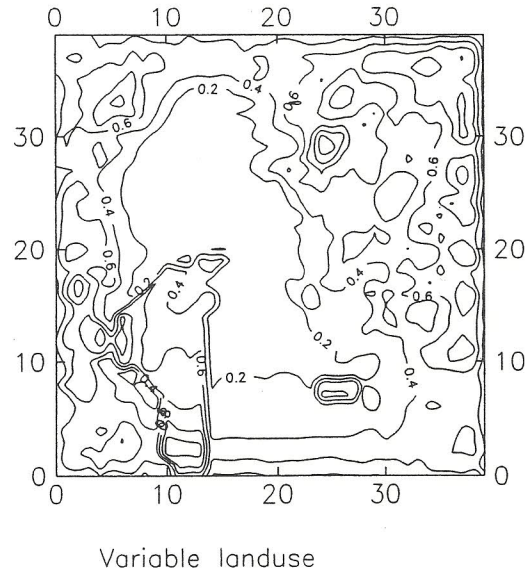

FIG. 10.8. As in Fig. 10.7 except for the variable land-use run as shown in Fig. 10.5.

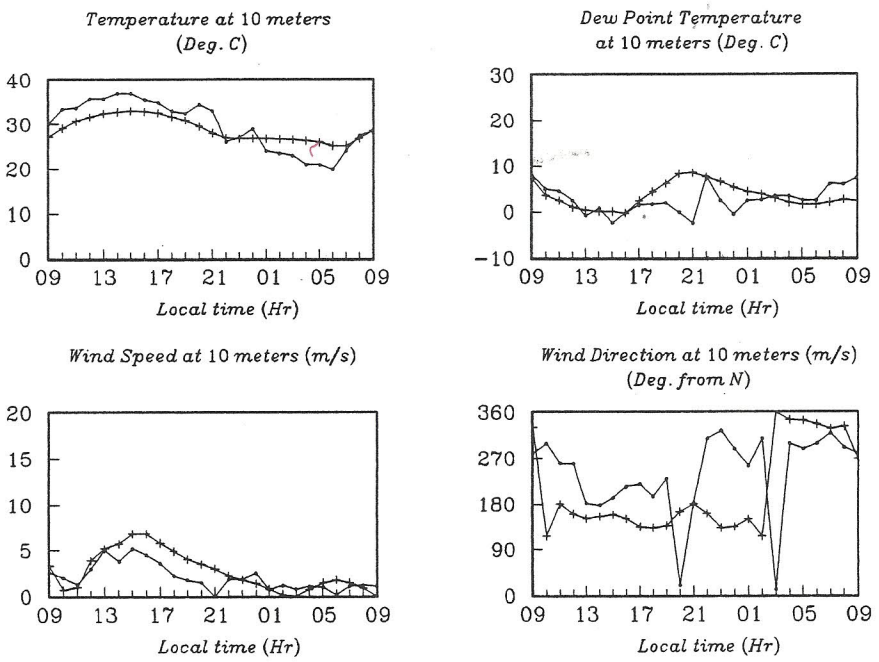

FIG. 10.9. Diurnal variation of (a) temperature, (b) dewpoint temperature, (c) wind speed, and (d) wind direction for both model (crosses) and observations (dots) at station S10. Units are indicated.

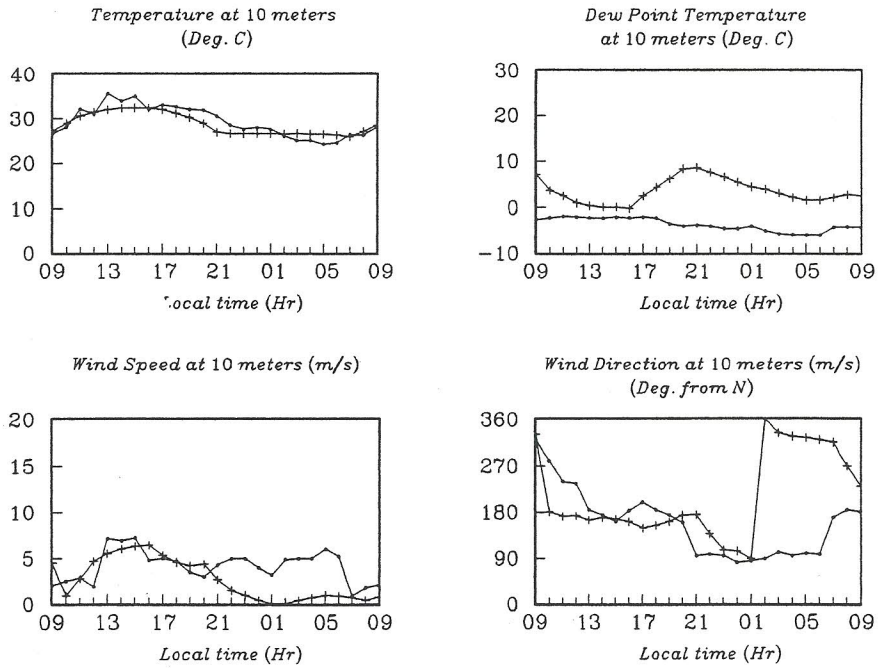

FIG. 10.10. As in Fig. 10.9 except at station S11.

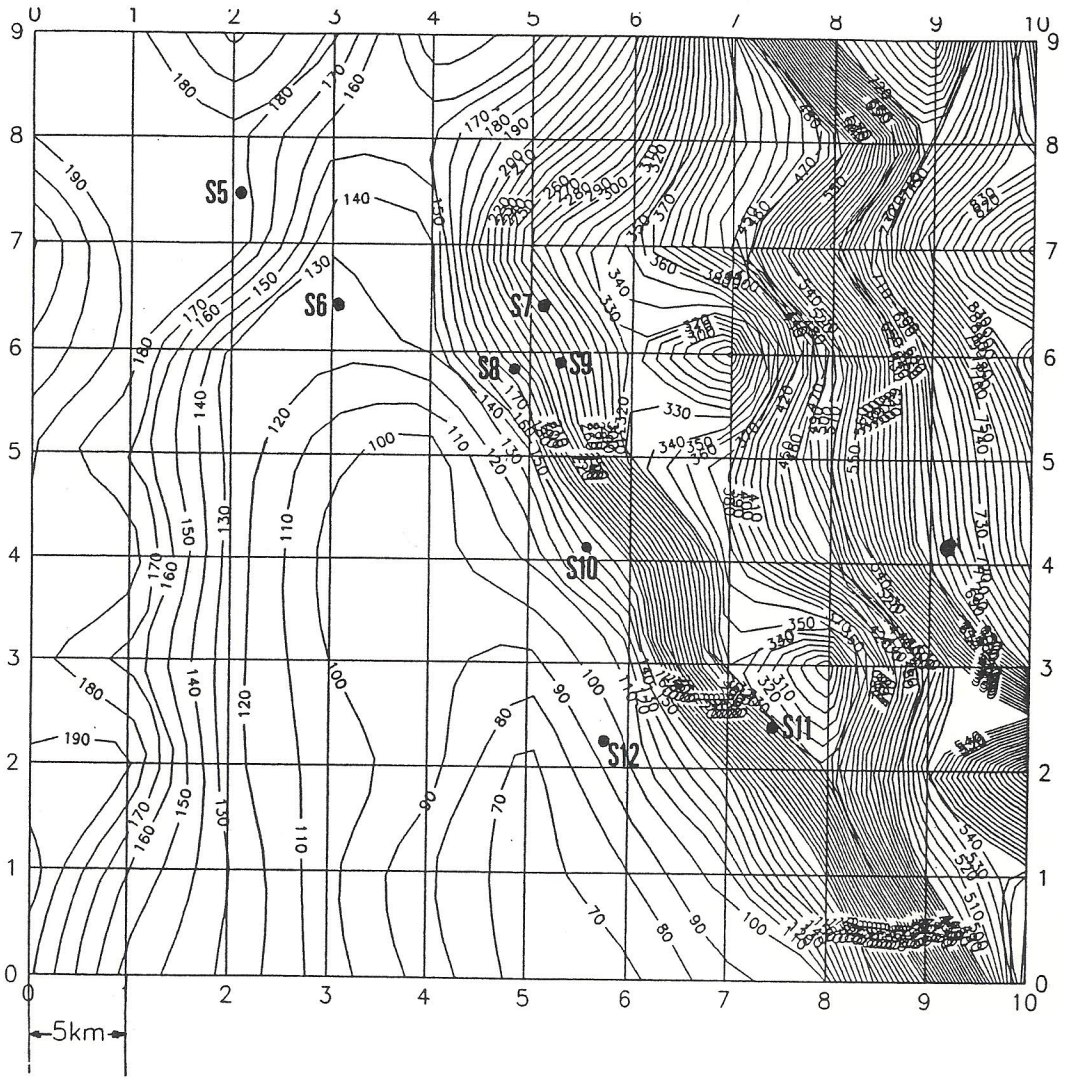

FIG. 10.11. Blowup of the topography at the neighborhood of stations S10, S11. Contour interval is 10 m.

(about two grid intervals), the model verification against observation is very different. This is particularly noticeable through the much drier and the stronger nocturnal wind speeds in S11. The model seems to represent the topography near S10 better. The blowup of the topography (Fig. 10.11) shows that a 5-km resolution will not suffice if differences between the two stations are required in the model simulation.

d. Moisture initialization

The initial surface moisture field at the first time step (t = 10 s) along with observed surface relative humidities are shown in Fig. 10.12. It indicates that the surface observed humidity is lower than that deduced from the radiosonde initialization. The lowest-level RH values from the radiosondes were 23%, 23%, 28%, and 41%, whereas the nearby observations show lower values near 15%. It was suggested that radiosonde RH measurements were less accurate than for the surface stations.

e. Vertical resolution

Figure 10.13 compares the model and the observations at upper-air station 1 for 1500 and 0300 PST on the upper and lower panels, respectively. The fields are (from left to right) wind speed, wind direction, and dry and dewpoint temperatures. As expected, the upper-level dewpoint inversion at approximately 7 km is not predicted, since the model resolution at that altitude is about 1.5–2 km. Another point of interest is the relatively weak upper-level wind intensities at both 0300 and 1500. These deviations are larger at night following 18 h of simulation and are attributed to the increase of the synoptic upper-level wind intensities

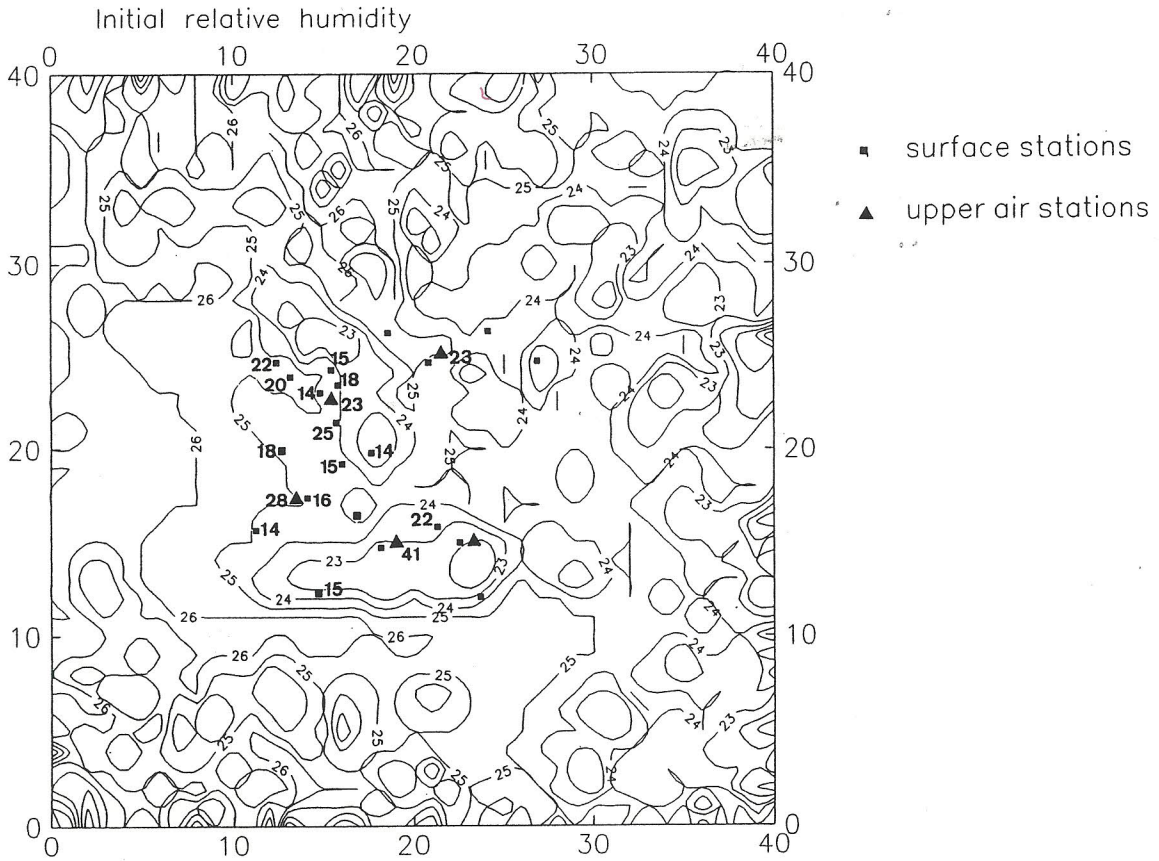

FIG. 10.12. Surface relative humidity field at first time step (10 s) along with the observed values at surface (squares) and upper-air (triangles) stations.

during the day. These were not accounted for in the constant lateral boundary summer run.

10.4. Winter phase II results

All five radiosondes were available for interpolating the initial winds as well as for updating the lateral boundary conditions each time step. For the time interpolation only, the radiosondes at 1000, 2200, and 1000 PST on 1–2 February 1986 were employed, that is, with a 12-h interval. Again, as in the summer, some of the model sensitivities are explored: subscale topographical features, lateral boundary conditions (BC), and vertical wind interpolation.

a. Subscale topography

Figures 10.14a and 10.14b show the model verification for the diurnal temperature variation, at stations S5 and S6, respectively. As indicated earlier, for the similar case in summer (Figs. 10.9 and 10.10) the observations differ widely, whereas the model predictions show similar diurnal variations. Figure 10.15 shows the topographical blowup of the area illustrating the very different exposure of S5 and S6, although their separating distance is about one grid length only. Obviously, higher horizontal resolution is required in the model in order to capture these subscale variations.

b. Lateral boundary conditions

In this case where a weak frontal passage was observed past midnight, the update of the lateral BC was found necessary, but insufficient, for a successful prediction. For instance, Figs. 10.16a and 10.16b show the model verification for the diurnal wind speed variation at station S4 with constant and variable lateral BC, respectively. The observed double peak wind increase after midnight associated with the frontal passage is in sharp contrast with the model wind weakening when a constant BC is employed (Fig. 10.16a). In the variable BC, however, the model does show some speed increase ($\sim$4 m s^{-1}), but this is still quite far from the observed values of about 7 m s^{-1}. Similarly, large deviation is noticed in the model wind direction at S3 (Fig. 10.17a) with a constant BC. This is considerably improved when the variable BC was employed (Fig. 10.17b).

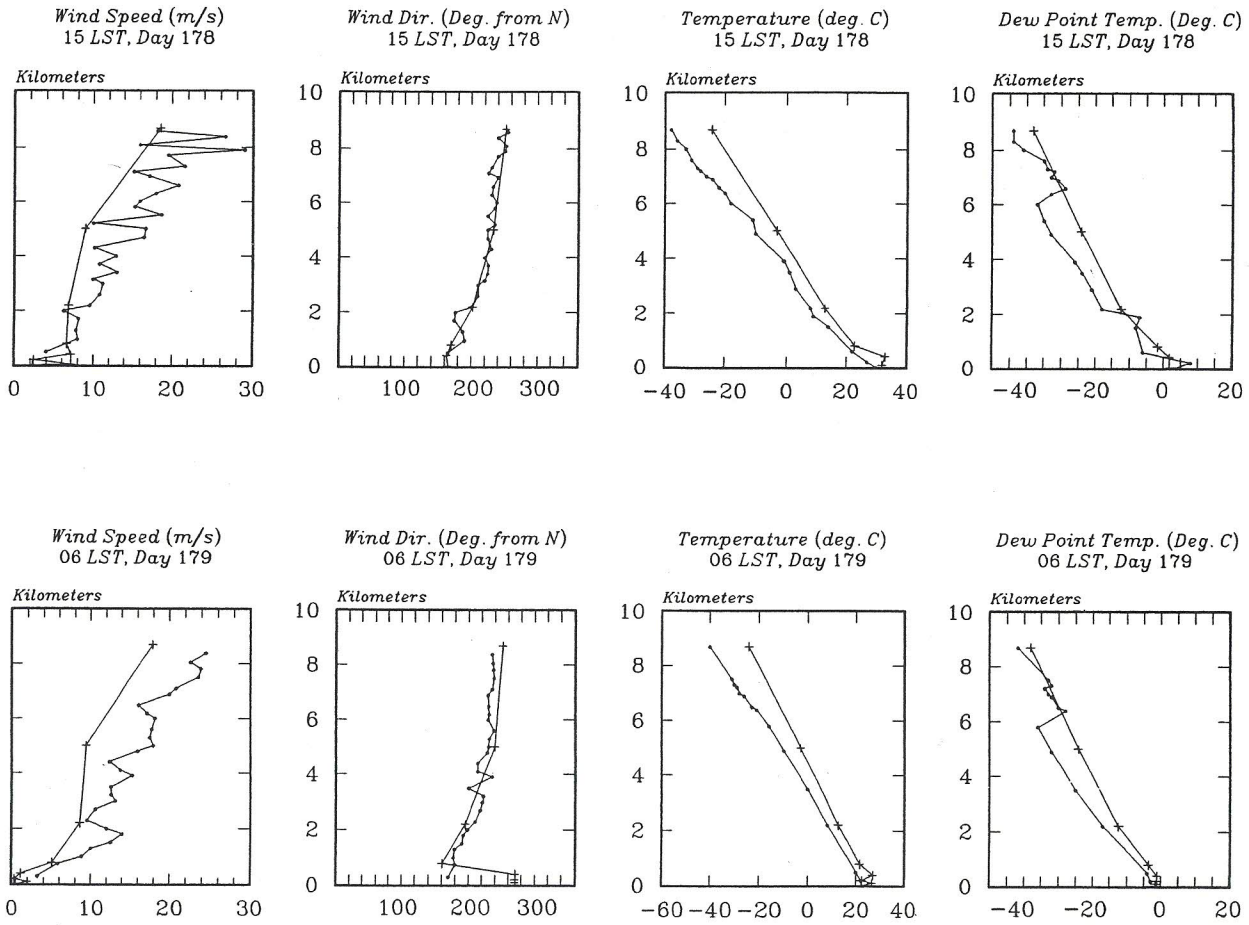

FIG. 10.13. Vertical profiles of (from left to right) wind speed, wind direction, temperature, and dewpoint temperature for both model (crosses) and radiosonde observations (dots). Upper and lower panels are for 1500 and 0300 PST, respectively. Units are indicated.

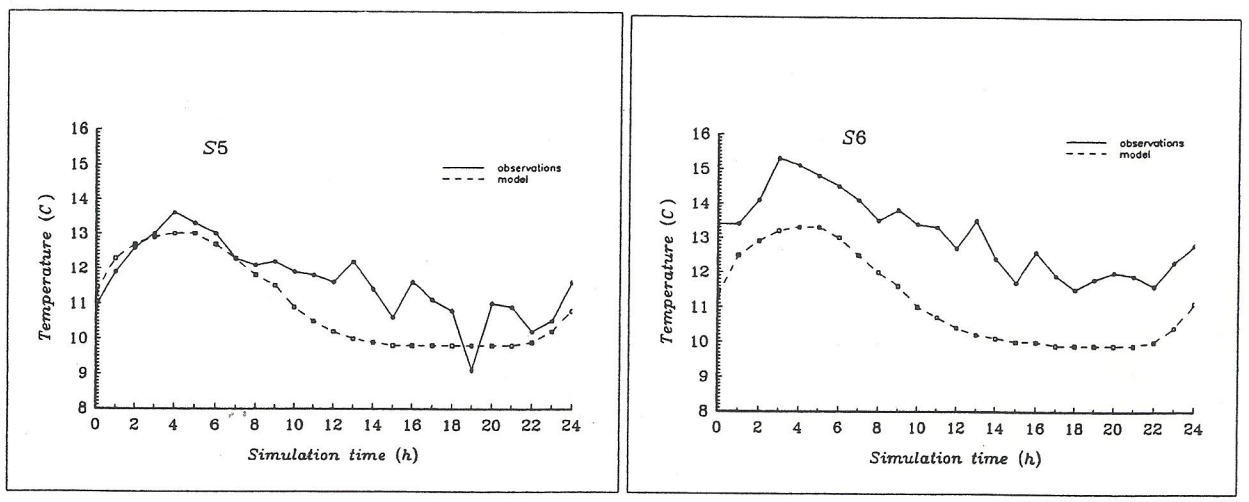

FIG. 10.14. Verification of diurnal temperature variations at stations (a) S5 and (b) S6. Observations (solid) and model (dashed) results are shown.

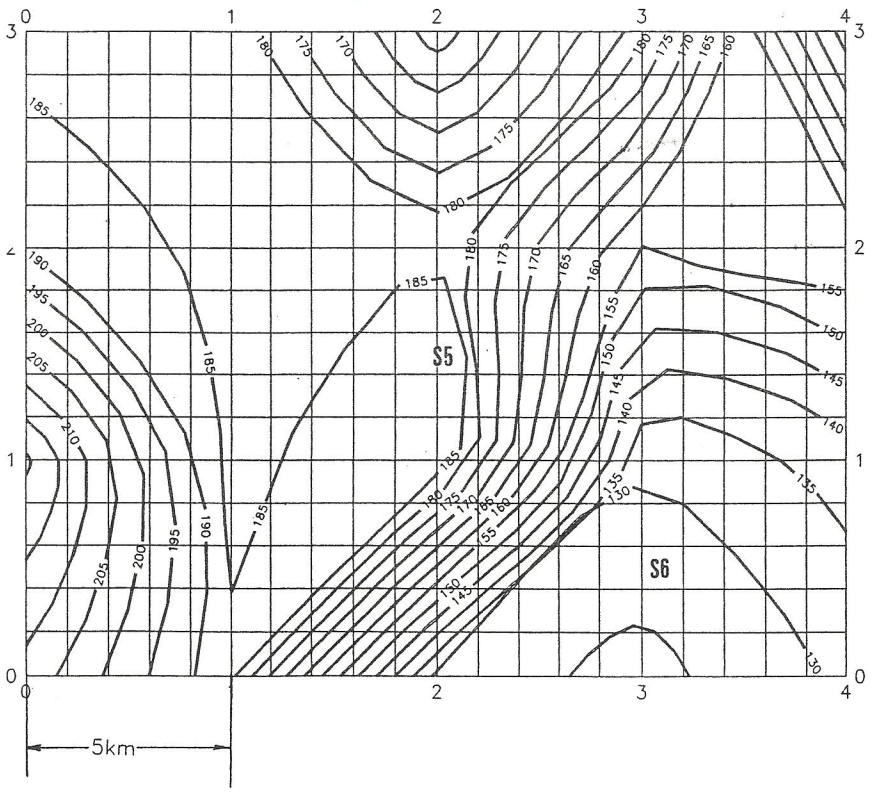

FIG. 10.15. Blowup of the topography in the neighborhood of stations S5 and S6. Contour interval is 5 m.

c. Vertical wind interpolation

When verifying model predictions we noticed that the way that vertical interpolation from the σ or p levels is performed is quite important, particularly near the surface. Figures 10.18a and 10.18b show the 2-m wind speed verification at station S4 with linear and logarithmic interpolations from 5 m, respectively. Indeed, the linear interpolation weakens the wind speed too much (Fig. 10.18a), whereas the logarithmic interpolation does well. As already discussed earlier (Fig. 10.16), the further deviations later into the simulation

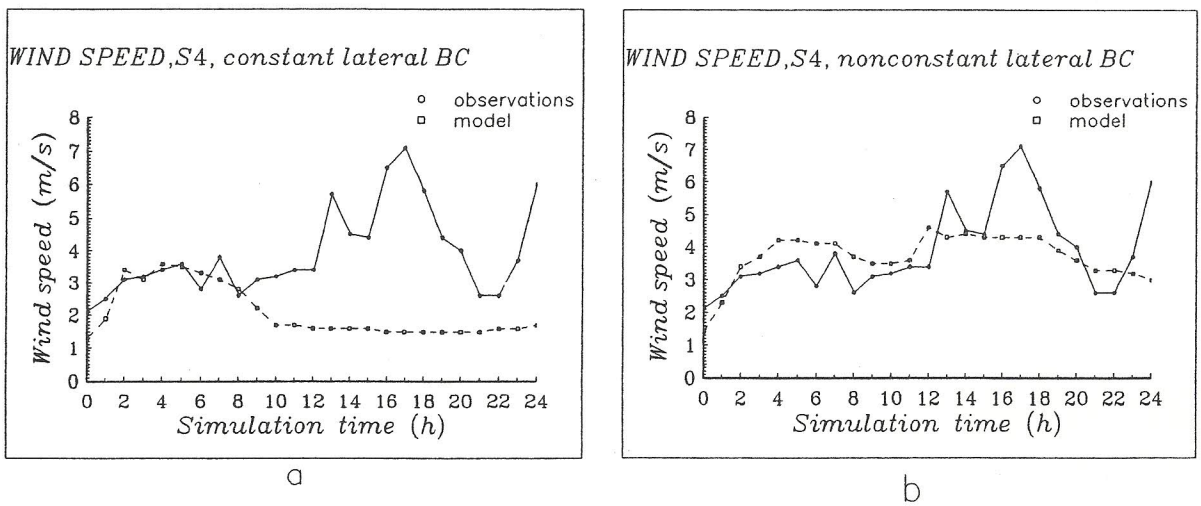

FIG. 10.16. Model verification for diurnal wind speed variation at station S4 with (a) constant and (b) variable lateral boundary conditions. Model (dashed) and observation (full) curves are drawn.

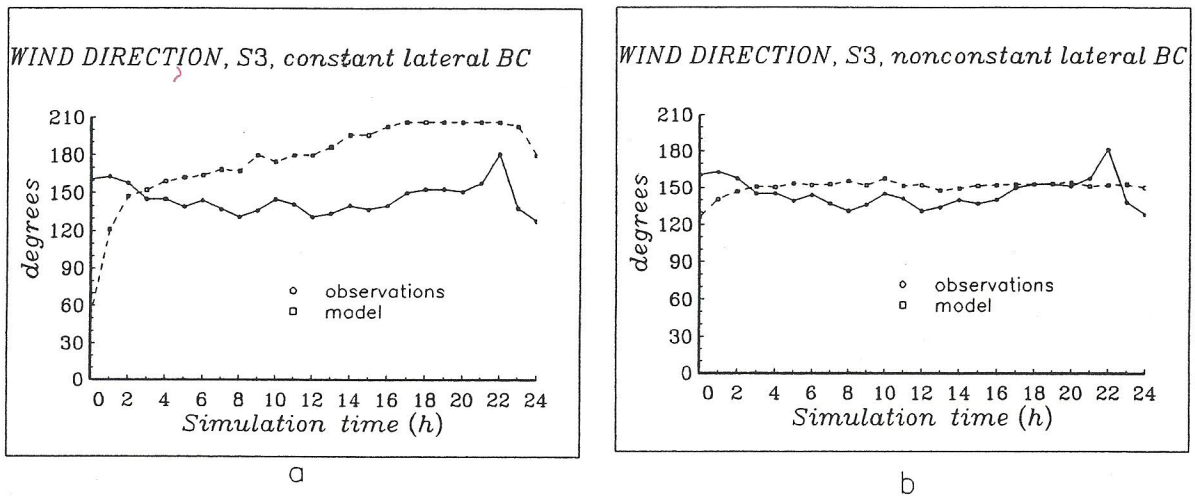

FIG. 10.17. As in Fig. 10.16, but for the wind direction at station S3.

are due to the constant BC that was employed in this simulation.

d. Spatial moisture variability

One of our findings is the large variability in the surface moisture verification. Figures 10.19a–h show the relative humidity verification at stations S1, S2, S3, S4, S5, S6, S14, and BS2. In the first four, agreement of prediction with observations is good, but this is not so for the four stations over the right panel. This is not surprising in light of the large spatial variability of surface moisture. Also, the geographical distribution for these two station groups is different (Fig. 10.5). The better predicted group is at the southwest part of the valley.

10.5. Separating the effects of terrain and surface fluxes

Stein and Alpert (1993) have recently suggested a method that allows the separation of the effects of various processes and their interactions in the model output. They showed that for n processes 2^n simulations are required for a complete separation. The method was applied to the 1500 PST wind vectors of the summer simulation where two processes were chosen: the surface fluxes and the topography. Each vector in the control run was decomposed into the four following vectors: terrain (**T**), fluxes (**F**), terrain–fluxes interaction (**TF**), and the residual vector mainly associated with the large-scale effect (designated by **LS**).

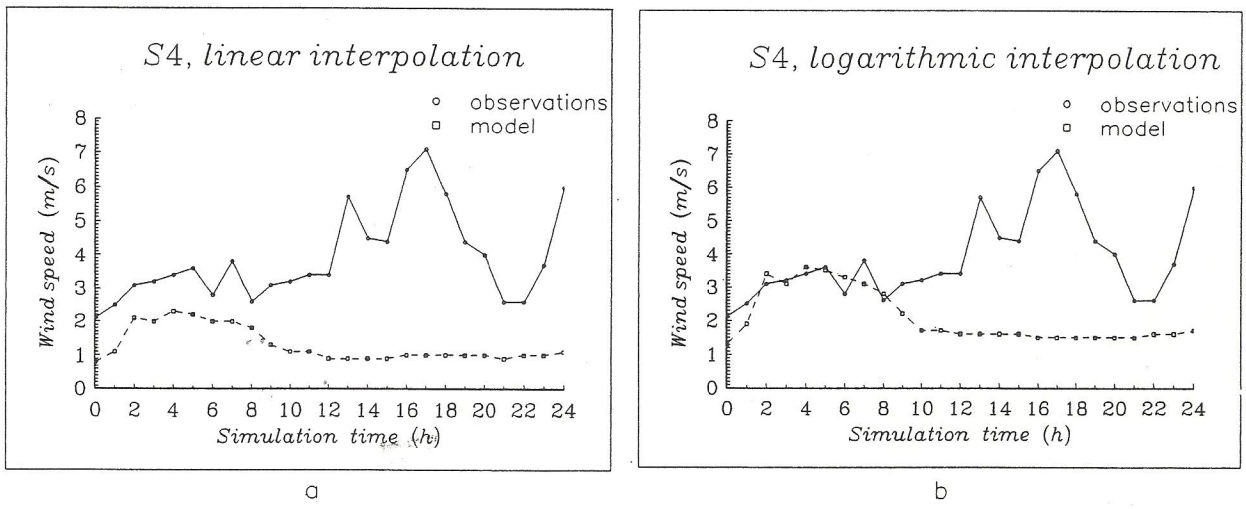

FIG. 10.18. Model verification for the 2-m diurnal wind speed at station S4 with (a) linear and (b) logarithmic interpolations from the 5-m model prediction. Model (dashed) and observation (full) curves are drawn.

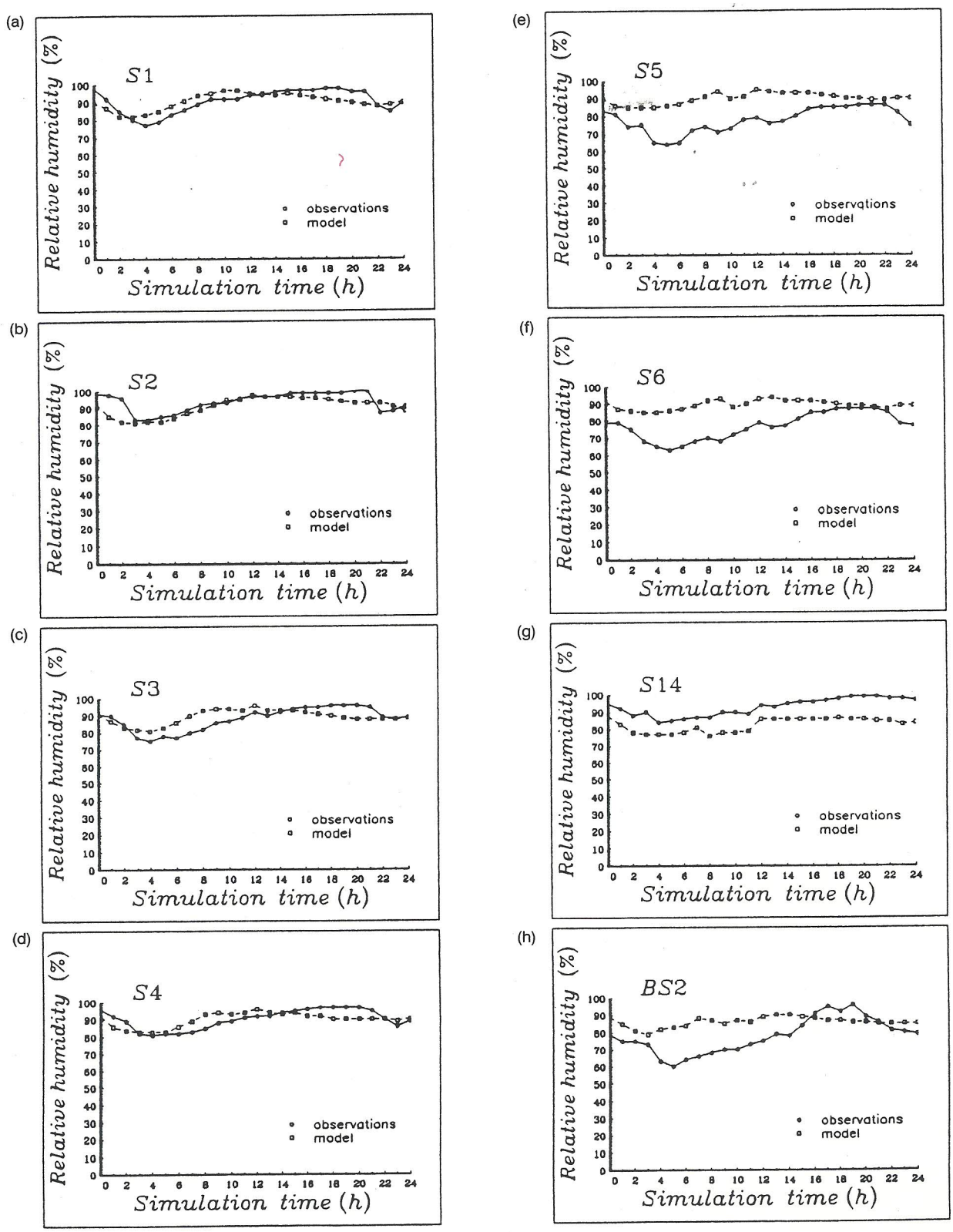

FIG. 10.19. (a)–(h) Model verification for diurnal variation of relative humidities at stations S1, S2, S3, S4, S5, S6, S14, and BS2. Model (dashed) and observation (full) curves are drawn.

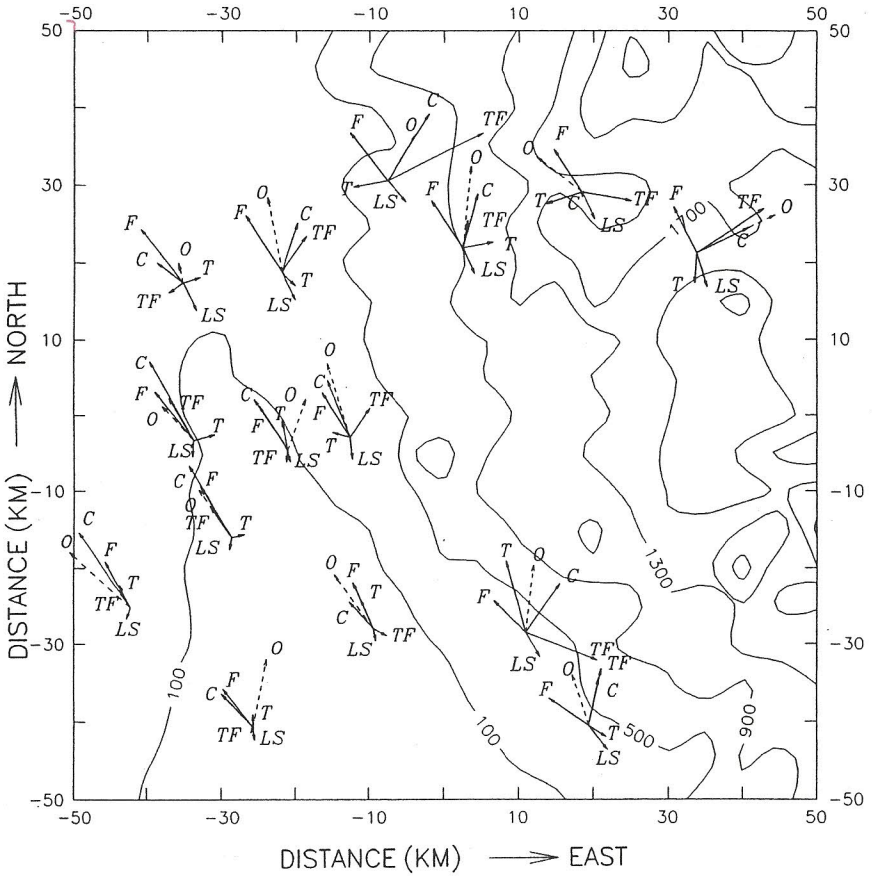

FIG. 10.20. Model domain 100 km × 100 km in the Sacramento Valley, California. Topographic contour interval is 400 m. Observed (**O**; dashed) wind vectors along with the control run result (**C**) for 1500 PST 27 June 1985 are plotted. Factor-separated wind vectors are topography (**T**), fluxes (**F**), topography-flux synergism (**TF**), and the residual large-scale (**LS**). The four contributions sum up to the control wind vector.

Figure 10.20 presents the factor-separated vectors in 15 locations where the observed wind was available. The observed wind was added for comparison with the control (**C**) result and is denoted by the **O** vector. One interesting result is that the synergistic **TF** contribution is dominant over the mountainous region, whereas at the Sacramento Valley the **F** contribution is dominant. This is not surprising since the **TF** represents the anabatic wind that is due to combined effect of thermal fluxes and sloping terrain. The **T** effect, however, represents only the mechanical effect and is relatively small at this time of the day. This method allows a better physical insight into the mechanisms responsible for the surface winds.

10.6. Conclusions

Our study shows that the high-resolution meso-β-scale simulations over Sacramento Valley, California, are highly sensitive to initial and boundary conditions. During summer, it was found that land-use variation can affect the Bowen ratio considerably, even to its doubling. It was also shown that initial surface moisture field from radiosondes is certainly insufficient and possibly inaccurate. During winter, the updating of the lateral BC was found crucial, but insufficient, for predicting the weak frontal passage at the early morning. Large spatial variability in moisture verification was found, and in both seasons subscale topographical features cause, as expected, significant deviations in the model verification.

Acknowledgments. We wish to thank the U.S. Army for the opportunity to use the unique WIND dataset for exploring model sensitivities and, in particular, R. Cionco, as well as the European Mesomet Panel. Special thanks are also due to Prof. Pearce for pursuing this subject.

APPENDIX

The PSU–NCAR Mesoscale Model

This meteorological model was developed by Anthes, Warner, and their colleagues at the National Center

for Atmospheric Research (NCAR) and The Pennsylvania State University (PSU). The version of the PSU–NCAR model that was used in the studies is described in Anthes et al. (1987) and Hsie (1987). The development below follows that description.

a. Equations

The momentum equations are given by

$$\frac{\partial p^* u}{\partial t} = -m^2\left(\frac{\partial p^* uum^{-1}}{\partial x} + \frac{\partial p^* vum^{-1}}{\partial y}\right) - \frac{\partial p^* u\dot{\sigma}}{\partial \sigma} - mp^*\left[\frac{RT_v}{(p^* + p_t\sigma^{-1})}\frac{\partial p^*}{\partial x} + \frac{\partial \phi}{\partial x}\right] + fp^* v + F_H u + F_V u$$

$$\frac{\partial p^* v}{\partial t} = -m^2\left(\frac{\partial p^* uvm^{-1}}{\partial x} + \frac{\partial p^* vvm^{-1}}{\partial y}\right) - \frac{\partial p^* v\dot{\sigma}}{\partial \sigma} - mp^*\left[\frac{RT_v}{(p^* + p_t\sigma^{-1})}\frac{\partial p^*}{\partial y} + \frac{\partial \phi}{\partial y}\right] - fp^* u + F_H v + F_V v,$$

where

$$p^* = p_s - p_t.$$

The continuity equation is

$$\frac{\partial p^*}{\partial t} = -m^2\left(\frac{\partial p^* um^{-1}}{\partial x} + \frac{\partial p^* vm^{-1}}{\partial y}\right) - \frac{\partial p^*\dot{\sigma}}{\partial \sigma}.$$

The vertical integral of the continuity equation is used to compute the time variation of p^*:

$$\frac{\partial p^*}{\partial t} = -m^2\int_0^1\left(\frac{\partial p^* um^{-1}}{\partial x} + \frac{\partial p^* vm^{-1}}{\partial y}\right)d\sigma'.$$

Then the vertical velocity in sigma coordinates is computed at each level in the model:

$$\dot{\sigma} = -\frac{1}{p^*}\times\int_0^\sigma\left[\frac{\partial p^*}{\partial t} + m^2\left(\frac{\partial p^* um^{-1}}{\partial x} + \frac{\partial p^* vm^{-1}}{\partial y}\right)\right]d\sigma'.$$

The thermodynamic equations are represented as follows:

$$\frac{\partial p^* T}{\partial t} = -m^2\left(\frac{\partial p^* uTm^{-1}}{\partial x} + \frac{\partial p^* vTm^{-1}}{\partial y}\right) - \frac{\partial p^* T\dot{\sigma}}{\partial \sigma} - \frac{RT_v\omega}{c_{pm}(p^* + p_t\sigma^{-1})} + \frac{p^* Q}{c_{pm}} + F_{HT} + F_{VT},$$

where $\omega = p^*\dot{\sigma} + \sigma\dfrac{\partial p^*}{\partial t}$.

Also note that

$$\frac{dp^*}{dt} = \frac{\partial p^*}{\partial t} + m\left(u\frac{\partial p^*}{\partial x} + v\frac{\partial p^*}{\partial y}\right)$$

and $c_{pm} = c_p(1 + 0.8q_v)$.

The hydrostatic equation and virtual temperature are used to compute the geopotential heights:

$$\frac{\partial \phi}{\partial \ln(\phi + p_t/p^*)} = RT_v\left(1 + \frac{q_c + q_r}{1 + q_v}\right)^{-1},$$

where $T_v = T(1 + 0.608q_v)$.

The physics closures on the subgrid are first order, and detailed boundary parameterization is according to the modeling of Blackadar (Zhang and Anthes 1982). A grid-scaled diffusivity is also included for stability.

b. Definitions of symbols

The symbols used in the quoted equations are generally standard. Only those with meanings specific to the particular model concerned are defined here:

$$m\text{—map factor}\left[= \frac{\sin\psi_1}{\sin\varphi}\left(\frac{\tan\psi/2}{\tan\psi_1/2}\right)^{0.716}\right],$$

where $\psi_1 = 30°$, $\psi = 90° - \varphi$, and φ is latitude. Suffix s denotes surface and t denotes top of model atmosphere.

c. Solution technique

The finite-difference methods use an Arakawa B staggered grid and approximately conserve mass, mo-

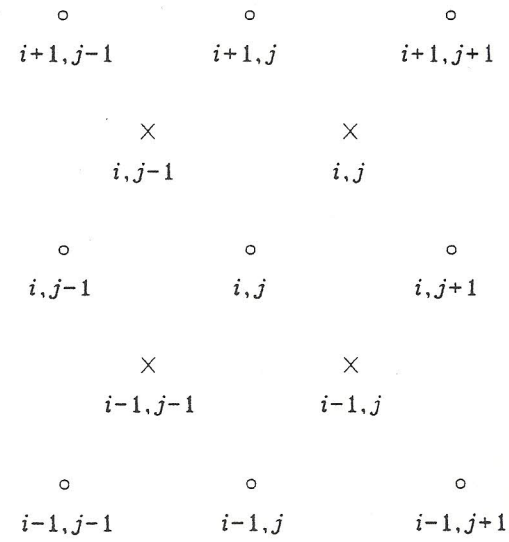

FIG. 10A.1. Depiction of dot points and offset cross points.

mentum, and total energy. The p^*u and p^*v variables are calculated at so-called dot points and all other variables are calculated at offset cross points, using $y(i)$, $x(j)$ indexing as shown in Fig. 10A.1.

A typical finite-difference equation is represented by the u component of the equations of motion:

$$\frac{\partial p^*u}{\partial t} \approx -m^2\left[\left(\bar{u}^x \frac{\overline{\overline{p^*u}^y}^x}{m}\right)_x + \left(\bar{u}^x \frac{\overline{\overline{p^*v}^x}^y}{m}\right)_y\right] - \frac{\delta\bar{\sigma}^{xy}\overline{p^*u}^{\sigma}}{\delta\sigma} - m\overline{p^*}^{xy}\overline{\phi_x}^y - \frac{mR\overline{T_v}^{xy}}{(1 + p_t/\overline{p^*}^{xy}\sigma)}\overline{p_x^*}^y + fp^*v + F_Hu + F_Vu.$$

Subscript coordinates represent two-point derivatives, overbars represent two-point averages per coordinate, and over brackets represent four-point operations:

$$\alpha_x = \frac{1}{\Delta s}[\alpha(i, j + {}^1\!/_2) - \alpha(i, j - {}^1\!/_2)]$$

$$\bar{\alpha}^x = \frac{1}{2}[\alpha(i, j + {}^1\!/_2) + \alpha(i, j - {}^1\!/_2)]$$

$$\widetilde{\alpha^x} = \frac{1}{4}[\alpha(i, j + 1) + 2\alpha(i, j) + \alpha(i, j - 1)].$$

The accuracy of the model was found to be sensitive to the form of the hydrostatic equation used. The best results were found by integrating the hydrostatic equation above to find ϕ at velocity levels.